The impact of turbulence on supernovae shockwaves

Loke Lönnblad Ohlin

Lund Observatory
Lund University

2018-EXA129

Degree project of 15 higher education credits
January 2018

Supervisor: Oscar Agertz

Lund Observatory
Box 43
SE-221 00 Lund
Sweden

Abstract

The momentum and energy injection from supernovae is one of the main feedback modes, and is therefore key to the understanding of galaxy evolution and star formation. However, due to low resolution, large scale galaxy simulations often have issues with accurately modelling supernovae, and therefore rely on sub-grid models. This is especially true for the injected momentum, where capturing the momentum generating adiabatic phase of SNe, although important, is impossible to self-consistently model in large scale simulations. Previous studies have shown that the final momentum injected only has a weak dependence on the surrounding density, and that the detailed structure of the interstellar medium (ISM) is at large irrelevant when considering the momentum. However these studies lacked accurate modelling of the turbulence in the ISM, and instead resorted to static models, where the velocities of the gas were ignored.

In this work, we start by retrieving a known semi-analytic solution of the early and important adiabatic Sedov-Taylor stage, responsible for most of the momentum generation. This solution is then compared to a series of full hydrodynamical simulations using an adaptive mesh refinement code, called RAMSES, with varying mean density of the surrounding ISM. With the inclusion of atomic cooling, the evolutionary stages of supernovae remnants are recovered, with the final momentum p found depending on the surrounding hydrogen density n as $p \propto n^{-0.15}$, in agreement with previous studies.

We then adopt a model of turbulence by Padoan & Nordlund (1999), which was calibrated to produce power spectra, density and velocity distributions based on the conditions in giant molecular clouds (GMCs). With this model of the surrounding ISM, the geometry of the SNe shocks changes drastically, preferring channels of less dense gas, leaving higher density filaments mostly intact. However the evolution of momentum and energy of the system still follows the same trend as in the homogeneous case, reaching a similar peak momentum. The momentum was found to decrease with time, which is not predicted in the homogeneous case, but the decay appears to be on longer time scales. This reaffirms the previous results, stating that the detailed structure of the ISM only has a negligible effect on the momentum and energy of the early stages of SNe. Nevertheless, the SNe does show a tendency of generating outflows of low density gas rather than affecting the high density regions, which could have further impacts on SFR and galaxy evolution as a whole.

Populärvetenskaplig beskrivning

Supernovor är några de kraftfullaste händelserna vi ser bland stjärnor. När stjärnor, mycket mer massiva än vår egen, bränner upp sitt bränsle tynar de inte bara bort, utan exploderar i vad vi kallar en Typ II supernova. På motsatta sidan kan lättare stjärnor i sina sista tillstånd som vita dvärgar fånga upp för mycket massa och explodera som Typ I supernovor. Båda dessa fallen har en stor betydelse för utvecklingen av galaxer. Utan dem hade inga grundämnen tyngre än järn existerat i de mängderna vi ser, då majoriteten av dessa endast kan skapas i den extremt varma explosionen. Supernovor är också viktiga i att skjuta ut gas från galaxer genom att skapa massiva vindar. Utan dessa vindar skulle stjärnor födas för snabbt och förbruka gaserna i galaxer. Detta skulle innebära att galaxer inte hade haft tillräckligt med gas för att fortsätta föda stjärnor än idag.

I och med supernovors påverkan på universumet vi ser, är det intressant för astrofysiker att förstå hur dessa explosiva händelser utvecklas. Men supernovor, som med mycket inom astronomi, utvecklas under väldigt lång tid. Därav kan observationer endast ge en ögonblicks bild, vilket begränsar vår tillgång till fysiken bakom dem. Därav använder astrofysiker ofta sig av datormodeller för att fylla i bilden, med högupplösta simuleringar som kan återskapa en detaljrik bild av supernovor, liksom andra aspekter av astronomi.

Men när större skalor inom astrofysiken simuleras, så som galaxer, så kan inte dagens datorer komma upp i en tillräcklig upplösning för att simulera supernovor utan att simuleringen tar för lång tid. Därför används oftast vad som kallas ”sub-grid modells”, för att inkludera supernovor även om upplösningen inte kommer ner i dem skalorna. För att skapa dessa modeller har tidigare studier simulerat supernovor på mindre skalor för att se hur de utvecklas i olika medier. Dessa simuleringar har tagit hänsyn till den omgivande gasen runt stjärnor, och sett att bland annat energin och rörelsemängden påverkas av mängden av denna gas. Men dessa simuleringar har hittills inte inkluderat gasens rörelser, utan använt sig av en stillbild på hur den borde se ut. I verkligheten rör sig den interstellära gasen slumpmässigt, i vad som kallas turbulens, och den gör så supersoniskt, det vill säga snabbare än ljudets hastighet. Denna turbulens innebär inte bara att gaserna rör sig, utan även att det bildas tjockare och tunnare skikt-liknande strukturer, som man kan se i t.ex. rök. Eftersom hur gasens rörelser påverkan på supernovor inte har undersökts än, så vet vi ännu inte hur markanta de är.

Projektet som har gjorts till denna rapport har försökt simulera supernovor i ett mer realistisk, rörligt medium än vad som har gjorts tidigare. Med dessa simuleringar visar vi att trots att supernovorna får annorlunda former, så påverkas inte den slutgiltiga energin eller rörelsemängden markant. Vi visar även att eftersom explosionen föredrar att färdas genom tunnare gas, så kan enskilda supernovor trycka bort den tunnare gasen, medan de lämnar kvar den tjockare regionerna. Detta kan påverka hur mycket gas som en enskild supernova skjuter ut, och därmed hur effektiva de är på att reglera stjärnformation.

Contents

List of Figures

List of Tables

Chapter 1

Introduction

Supernovae (SNe) are a key factor in the evolution of the Universe. These explosions, resulting from the core-collapse of massive stars (type II) or the sudden eruption of white dwarfs exceeding the Chandrasekhar mass limit (type Ia), are not only the main source of iron and heavier elements, but also drives the supersonic turbulence in the ISM and galactic outflows of gas with the momentum injection. Therefore, understanding these events is key for accurate modelling and understanding of galaxies and larger structures, as for example the injected momentum is an important factor in star formation (McKee & Ostriker 2007; Mac Low & Klessen 2004), with the resulting turbulence causing over-densities necessary, while the outflows of gas regulates the star formation rate.

The typical length scale of supernovae remnants are of the order of parsecs, and this is the scale where the momentum and energy is deposited. However most galactic and cosmological simulations do not reach high enough resolutions to properly model the feedback from SNe, and therefore rely on sub-grid models for the momentum injection (Agertz et al. 2013; Stinson et al. 2006). This takes the energy and momentum injection as crucial free parameters, requiring extensive knowledge of the evolution of supernovae to accurately model galaxy formation and evolution.

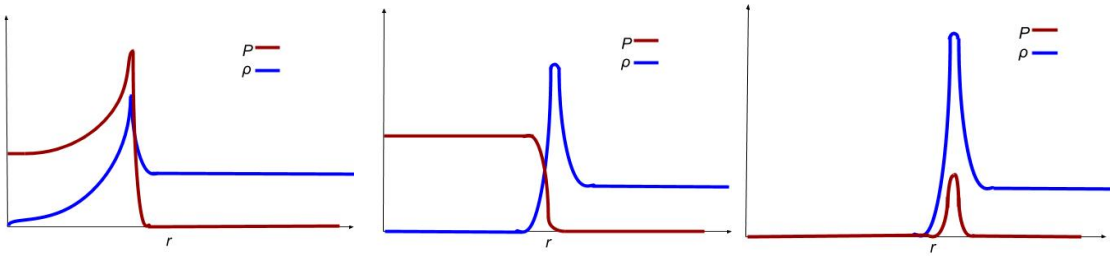

(a) ST (b) PDS (c) MCS

Figure 1.1: An illustration of the pressure P (red) and density ρ (blue) profiles with the radius r from the centre on the x-axis of the Sedov-Taylor (ST), Pressure driven snowplough (PDS) and momentum conserving snowplough stages (MCS).

A simple picture of the evolution of a supernova in a homogeneous medium, specifically its shockwave and resulting remnant can be separated into four stages (see Kim & Ostriker 2015; Shu 1991, chap. 17). The first is the stage of free expansion, where the supernova generates a shockwave that moves at a constant velocity until it has swept up enough interstellar mass that the shock is no longer dominated by the ejecta from the supernova. At this point the shock transitions into the second stage. This so called Sedov-Taylor (ST) stage, roughly follows the analytic solution developed independently by the scientists giving its name, see the illustration in figure 1.1a. Here the shock bubble is driven via thermal expansion, with only energy losses via adiabatic cooling being non-negligible. This is because the interior of the bubble has typical temperatures of $T > 10^6$ K, where radiative cooling is largely inefficient. However as the work done by the adiabatic expansion causes a decrease of thermal energy density and therefore temperature. At some point the bubble reaches the lower temperatures ($T \sim 10^6$ K) where collisional processes suddenly becomes more efficient (Shu 1991). At this time ($t_{ST} \sim 10$ kyr), the SN remnant transitions into the third phase, the significant radiation loss from collisional cooling causes a cool dense shell to form just behind the shock front. This shell is pushed forward by the still hot, high pressure in the hot interior of the bubble, see figure 1.1b. After some time ($\sim 4 - 5t_{ST}$), the cooling causes the inside pressure to drop to the point that it is comparable to the outside pressure (figure 1.1c). In the resulting fourth and final stage the shock is only pushed forward by the momentum it has accumulated during its evolution. The last two stages are referred to as the pressure driven and momentum conserving snowplow phases (PDS and MCS), named by their main source of propulsion. This general picture holds for all types of SNe, as differences in energy and chemical composition generally only affect the time scale and extent of each phase, especially past the stage of free expansion where the shock is dominated by mass from the surrounding ISM.

As indicated earlier, the multi-stage nature of a supernova blast results in inaccurate results for inadequate resolutions, as often seen in large scale models. The most glaring of these is the overcooling problem (Stinson et al. 2006; Creasey et al. 2011). Here the the lack of time and spatial resolution does not allow for the Sedov-Taylor and the pressure driven snowplow stages to be captured accurately. The result of this is that these stages are cooled too fast resulting in lower momentum, as this is mostly gained during the ST and PDS stages. For this reason, several simulations have been done to study SN shocks in great detail (Martizzi et al. 2015; Kim & Ostriker 2015; Thornton et al. 1998; Haid et al. 2016) in order to parametrise how the energy and momentum injection from SNe depend on environmental factors, and provide accurate sub-grid models.

It has been shown that the simple model of SNe gets a more complicated when the diversity of the ISM is accounted for. Different densities of the surrounding medium affect the cooling as $\sim n^2$, and with different elements (such as oxygen and carbon) the cooling can be even more efficient. A higher surrounding density and/or metalicity then causes the shocked bubble to cool faster, causing the transitions between the ST, PDS and MDS to happen earlier, and decreasing the total energy and momentum injected into the ISM (Thornton et al. 1998).

The evolution of SNe gets complicated further by the fact that the ISM in not ho-

mogeneous. In fact it is better described by several thermodynamical phases (McKee & Ostriker 1977); a hot ionized phase ($T \sim 10^6$ K, $n \sim 10^{-2}$ cm^{-3}), a warm phase ($T \sim 10^4$, $n \sim 10^{-1} - 10^0$ cm^{-3}) and cold molecular clouds or GMC's ($T \sim 10^2$, $n_H \sim 10^1 - 10^2$ cm^{-3}). These phases are partly caused (and therefore subject to) turbulence due to supernovae and gravitational instabilities (with other processes, such as UV- background radiation causing heating). Within the GMC's the turbulence causes velocity dispersions proportional to the size of the cloud (Larson 1981), such that for a cloud on the scale of 10-100 pc we expect a dispersion of ~ 5 km/s.

As the ISM cannot be considered homogeneous, a SN shock will encounter different densities, pressure and temperatures in different directions. This could have implications on the supernova, as the Sedov-Taylor phase is dependent on the pre-shock (i.e outside) values of pressure, density and velocity, and as the extent of the pressure driven snowplow phase is limited by the outside pressure. This results in a non-spherically symmetric propagation, with the shock moving slower in denser volumes. In spite of these dependencies, the resulting momentum and energy have been shown to only change moderately if at all in hydrodynamical models compared to their equivalent homogeneous models (Martizzi et al. 2015; Kim & Ostriker 2015). However, in both of these studies the kinematics of the supersonic turbulence in the ISM was partly ignored. In Kim & Ostriker (2015), the different phases of the turbulence where generated using thermal instabilities, whereas Martizzi et al. (2015) adopted a static model, assuming a static log normal density distribution, matching a Kolmogorov power spectrum $E(k)\mathrm{d}k \propto k^{-5/3}\mathrm{d}k$, where k is the wavenumber. The static ISM was justified by assuming that the velocities of the turbulence was negligible compared to the velocity of the supernova shockwave in its earlier stages where, as previously mentioned, most of the evolution of the momentum occurs.

The assumption that the early stages of supernovae are not affected by turbulence has been tested by Haid et al. (2016), where a one dimensional analysis has found that the inclusion of supersonic turbulence increased the total injected momentum from SNe by 16% to ~ 100%, depending on the Mach number of the turbulence. The higher momentum injection may have been caused by the lower amounts of swept up mass which were found for higher Mach numbers, as the extent of the supernovae shockwaves depend the cooling, which is less efficient for low densities, resulting in higher momentum injection. However no such conclusions were made by Haid et al. (2016).

On the point of turbulence, one usually differentiates two types of turbulence: solenoidal (divergence-free) turbulence, where the turbulence tends to form small scale vortices, and compressive (or curl-free) turbulence. In supersonic turbulence, both of these can be prevalent (Mac Low & Klessen 2004), however produced power spectra differ depending on which is dominating the driving. In solenoidal dominated turbulence, one expects a spectrum as the one used in Martizzi et al. (2015), $E(k)\mathrm{d}k \propto k^{-5/3}\mathrm{d}k$, while compressive turbulence generates a power spectrum as $E(k)dk \propto k^{-2}\mathrm{d}k$ (Federrath 2013; Mac Low & Klessen 2004; Burgers 1948). The turbulence of the interstellar medium is inevitably going to be a combination of both solenoidal and compressive driving. However compressive dominated supersonic turbulence has a fractal dimension closer to those observed in GMC (Roman-Duval et al. 2010; Federrath 2013), which reflects a structure closer to sheets of

high density, with more volume of low density. These high density sheets surrounded by low density regions could have an impact on the evolution of SNe, as the shock bubble expands along the path of least resistance. The model of turbulence used by Martizzi et al. (2015), which produces a higher, more space filling fractal dimension, may not fully capture this type of expansion.

Another point is that Martizzi et al. (2015) ignored the kinematic aspect of the supersonic turbulence. While this could be reasonable as the velocities of the turbulence are much lower than that of a supernova, the full impact of self consistent supersonic turbulence has not been tested. Studies are required in order to assure that the final momentum injected in the ISM is the same regardless of the stochastic nature of the turbulence. This is exaggerated by the several instabilities that can occur at the interface of two different mediums, i.e the supernovae shock front and the outside medium. These include Rayleigh-Taylor instabilities (Sharp 1984), where the boundary between the shock and ISM is distorted, and nonlinear thin shell- instabilities, which can occur in the boundary between the differing densities of the shock and the ISM.

If two supersonic shocks collide, in this case the supernova and the turbulent ISM, a number of events could happen. The most basic impact could be that the collision causes an increase in temperature, as kinetic energy is converted to thermal, and subsequently cools, lowering the injected momentum. Another could be that the shock front gets punctured, resulting in a decrease of pressure within the bubble as it reaches equilibrium with the ISM, which would drastically change the evolution of the SNe. These two possibilities might have an negligible effect, but should occur in realistic turbulent flows, and the effect of these on supernovae has not been studied in detail.

The effects of the plethora of possible events that may affect supernovae might not be significant. If, for example, they only occur or are impactful at the momentum driven snowplow stage, not much is changed in the energy and momentum output, as reasoned by (Martizzi et al. 2015). Conversely, if it's found that a turbulent medium has effects on supernovae in their early times, as in the Sedov-Taylor or pressure driven snowplow stages, changes in kinetic energy or momentum may be significant enough to alter supernovae's impact on the ISM. In this work we investigate whether the impact of the kinematic aspect of turbulence is in fact negligible as stated by Martizzi et al. (2015); Kim & Ostriker (2015), or if it has to be accounted for in future simulations involving supernovae.

Chapter 2

Methods

To model the shocks generated by SNe, three methods were used.

1. **Semi-analytical solution:** Here the known semi-analytical solution for the energy conserving Sedov-Taylor (ST) stage is recovered by solving a set coupled ODE's, described fully in section 2.1. The results from this are then used to benchmark the full hydro dynamical numerical simulations.

2. **Numerical simulations in homogeneous media:** This step used hydrodynamical simulations to model the resulting explosion of supernovae in homogeneous media of varying density. Using the results from the semi-analytical solution as benchmarks, the resolution required to adequately model the shock-wave is considered and the resulting energy and momentum found is then compared with the results found in Kim & Ostriker (2015). This method is detailed in section 2.2.2.

3. **Numerical simulations in turbulent media:** Finally, with recovered known solutions to the evolution of SNe remnants, the novel simulations of supernovae in turbulent media are produced, as outlined in section 2.2.3.

2.1 Semi-analytical solution to the ST-stage

The analytic solution was based on a known model summarised below (for details see Shu 1991). The governing hydrodynamical Euler equations, i.e mass, momentum and energy conservation for a spherical symmetric explosion from a point source can be written as

$$\frac{\partial \rho}{\partial t} + \frac{1}{r^2}\frac{\partial}{\partial r}(r^2 \rho u) = 0, \tag{2.1}$$

$$\frac{\partial u}{\partial t} + u\frac{\partial u}{\partial r} = -\frac{1}{\rho}\frac{\partial P}{\partial r}, \tag{2.2}$$

$$\frac{\partial}{\partial t}\left[\rho\left(\epsilon + \frac{1}{2}u^2\right)\right] + \frac{1}{r^2}\frac{\partial}{\partial r}\left[r^2 \rho u\left(\epsilon + \frac{P}{\rho} + \frac{1}{2}u^2\right)\right] = 0, \tag{2.3}$$

where ρ, P, u, ϵ are the density, pressure, velocity and specific internal energy at position r at time t. These equations are only valid for a spherically symmetric shockwave and assume no energy loss outside of adiabatic expansion, which is the condition for the ST-stage in a spherically symmetric homogeneous medium.

A solution to these coupled ODEs can be derived using self-similar arguments. When doing this, one can define a dimensionless variable ξ as

$$\xi(r,t) = r\left(\frac{\rho_1}{Et^2}\right)^{1/5}, \tag{2.4}$$

where E the energy deposited in the point and ρ_1 is the density of the pre-shock gas. The position and value of the velocity of the shock are then given by

$$r_{sh} = \xi_0\left(\frac{Et^2}{\rho_1}\right)^{1/5} \tag{2.5}$$

$$U_{sh} = \frac{2}{5}\xi_0\left(\frac{E}{\rho_1 t^3}\right)^{1/5}, \tag{2.6}$$

where $\xi_0 = \xi(r_{sh})$, which needs to be calibrated for the correct solution. With ξ, and assuming an adiabatic equation of state, eqs.(2.1)-(2.3) can be written as

$$-\xi\frac{\mathrm{d}\alpha}{\mathrm{d}\xi} + \frac{2}{(\gamma+1)}\left[3\alpha v + \xi\frac{\mathrm{d}}{\mathrm{d}\xi}(\alpha v)\right] = 0, \tag{2.7}$$

$$-v - \frac{2}{5}\xi\frac{\mathrm{d}v}{\mathrm{d}\xi} + \frac{4}{5(\gamma+1)}\left(v^2 + v\xi\frac{\mathrm{d}v}{\mathrm{d}\xi}\right) = -\frac{2}{5}\left(\frac{\gamma-1}{\gamma+1}\right)\frac{1}{\alpha}\left(2p + \xi\frac{\mathrm{d}p}{\mathrm{d}\xi}\right), \tag{2.8}$$

$$-2(p+\alpha v^2) - \frac{2}{5}\xi\frac{\mathrm{d}}{\mathrm{d}\xi}(p+\alpha v^2) + \frac{4}{5(\gamma+1)}\left[5v(\gamma p + \alpha v^2) + \xi\frac{\mathrm{d}}{\mathrm{d}\xi}[v(\gamma p + \alpha v^2)]\right] = 0, \tag{2.9}$$

with the normalised variables

$$\alpha(\xi) = \rho(r,t)/\rho_{sh} = 1 \quad \text{for} \quad \xi = \xi_0, \tag{2.10}$$

$$v(\xi) = \frac{r_{sh}}{r}u(r,t)/u_{sh} = 1 \quad \text{for} \quad \xi = \xi_0, \tag{2.11}$$

$$p(\xi) = \left(\frac{r_{sh}}{r}\right)^2 P(r,t)/P_{sh} = 1 \quad \text{for} \quad \xi = \xi_0, \tag{2.12}$$

and the requirement

$$\frac{32\pi}{25(\gamma^2-1)}\int_0^{\xi_0}[p(\xi) + \alpha(\xi)v^2(\xi)]\xi^4\mathrm{d}\xi = 1, \tag{2.13}$$

for conservation of total energy, where γ is the adiabatic exponent. For a more detailed description, see Shu (1991).

In this thesis, the coupled ODE's (2.7)-(2.9) were solved such that $\mathrm{d}v/\mathrm{d}\xi$ was expressed independently of $\mathrm{d}\alpha/\mathrm{d}\xi$ and $\mathrm{d}p/\mathrm{d}\xi$

$$\frac{\mathrm{d}v}{\mathrm{d}\xi} = \frac{5}{4}\frac{\left(\frac{\gamma+1}{\gamma-1}\alpha v - \left[\left(\frac{4v}{5(\gamma+1)} - 1\right) - \frac{4\gamma v}{5(\gamma^2-1)} + \frac{2/5+\gamma}{\gamma-1}\right]\alpha v^2 - \frac{6}{5}(\frac{2\gamma v}{\gamma+1} - 1)p\right)}{\frac{1}{\gamma+1}\left(\gamma p + 2\alpha v^2 - \frac{\gamma}{\gamma-1}2\alpha v^2\right) - \left(1 - \frac{\gamma+1}{\gamma-1}\right)\alpha v - \frac{\gamma+1}{2(\gamma-1)}\alpha}. \tag{2.14}$$

This was then solved by a fourth order Runge-Kutta (RK4), stepping backwards from $\xi = \xi_0$, for a given ξ_0. In each step $\mathrm{d}v/\mathrm{d}\xi$ was calculated and then used to find $\mathrm{d}\alpha/\mathrm{d}\xi$ and $\mathrm{d}p/\mathrm{d}\xi$, which could be expressed as

$$\frac{\mathrm{d}\alpha}{\mathrm{d}\xi} = -\frac{\frac{6}{(\gamma+1)\xi}\alpha v - \frac{2}{\gamma+1}\alpha\frac{\mathrm{d}v}{\mathrm{d}\xi}}{\frac{2}{\gamma+1}v - 1} \tag{2.15}$$

$$\frac{\mathrm{d}p}{\mathrm{d}\xi} = -\frac{2}{5}\left(\frac{2}{\gamma+1}v - 1\right)\frac{\mathrm{d}v}{\mathrm{d}\xi} - \left(\frac{4}{5(\gamma+1)}v - 1\right)\frac{v}{\xi} - \frac{4(\gamma-1)}{5(\gamma+1)}\frac{p}{\alpha\xi} \tag{2.16}$$

The program solved the ODE's for different ξ_0's (increased by increment steps) and then calculated the discrete version of (2.13) for the given ξ_0 until it is equal to 1 within a tolerance of 0.0001. No advanced scheme was used to find ξ_0 as eq. (2.13) is monotonically increasing, and the value is known to be around $\xi_0 \approx 1.15$ (Shu 1991). With the correct ξ_0 the RK4 scheme was used again and the solution is converted into the physical normalised variables (i.e ρ/ρ_{sh} etc.), and later used to validate the full hydrodynamical numerical simulations. The results from this section are shown in section 3.1.

2.2 Numerical Simulations

2.2.1 RAMSES

For the hydrodynamical simulations, the program RAMSES (Teyssier, R. 2002) was used. RAMSES uses the Godunov finite volume method (Godunov 1959) for solving the more general case of the Euler equations shown in equations (2.1)-(2.3) on a Cartesian grid, with optional modules to solve physics as magnetic and gravitational forces, cooling of gas, etc. RAMSES also utilizes an adaptive mesh refinement to speed up computational time by only refining to a high degree regions of interest. At every time-step the spatial grid is updated and cells are marked for refinement if certain requirements are met. The requirement used in this project looks at the interface between a cell and its neighbour and interpolates a gradient of some variable ∇y. If the normalised value of this is greater than a limit set by the user, the cell and its neighbours are marked for refinement and subsequently divided into 8 child cells. This is done from a minimum level, which is applied to the entire volume, to a maximum level for the regions of most interest. At each level l the resolution is $\mathrm{d}x = L/2^l$, where L is the side length of the simulation box.

For the reasons stated above, RAMSES is widely used in the computational astrophysics community, and has had several astrophysical routines added, such as models for star

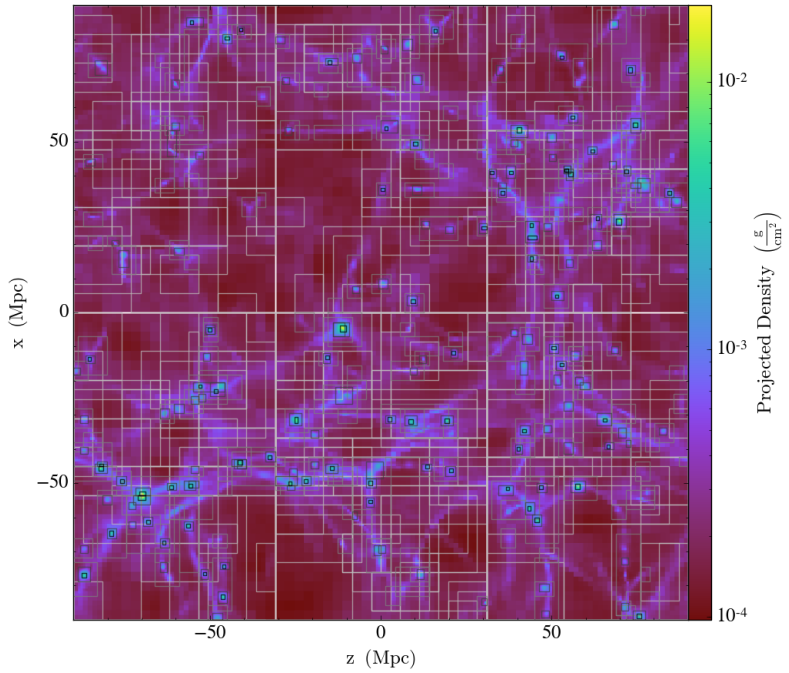

Figure 2.1: Illustrative figure of the adaptive grid used in RAMSES. As can be seen, in this case regions of high density are well refined, while low density regions left fairly un-refined. Taken from `http::://yt-project.org`

formation, stellar feedback, radiative pressure and background radiation (Agertz et al. 2013). For the purposes of this thesis, the gravity and hydrodynamical solvers were used, as well as the gas cooling module, which takes the density, metalicity and temperature for each cell, and calculates the energy loss from radiative cooling based on a pre-calculated table.

2.2.2 Homogeneous Medium

For SNe in homogeneous medium, a parameter space was explored and compared to the results found in Kim & Ostriker (2015). The medium was initialised in a box of side length $L = 100$ pc, with hydrogen number densities $n = 100, 10$ and 1 cm^{-3}, fixed temperature $T_0 = 10^4$ K and metalicity $Z = Z_\odot$. As described earlier, $n = 100, 10$ would correspond to the typical densities of GMCs at, while $n = 1$ are more in line with the surrounding hot ionized gas. The temperature chosen is consistent with Martizzi et al. (2015); Kim & Ostriker (2015) and while not realistic for GMCs, it would cool fast in the dense media. From this, the density and pressure where calculated as $\rho = nm_H/X$, $P = \gamma\rho k_b T/(m_H\mu)$, where X, μ are the hydrogen fraction and mean molecular weight respectively, and m_H the mass of a hydrogen atom. For all densities the resolution was varied to see how well the supernova was modelled, comparing to the semi-analytical solution derived earlier and the

results from Kim & Ostriker (2015). The condition for higher resolution was set such that neighbouring cells with $\nabla P > 0.1$ (normalised) were refined.

The supernova was initialised by depositing thermal energy $E = 10^{51}$ erg into a volume $\mathrm{d}x^3$, where $\mathrm{d}x$ is the smallest resolved length. This is the canonical value for the energy of supernovae, given from the ejection of $1\mathrm{M}_\odot$ with velocity of 10^4 km/s (Shu 1991). This came with an added density $\rho_{SN} = \rho$ evenly distributed in the small box. In this box, a scalar was added, which advects passively, not affecting the other variables. The corresponding scalar field acts like a "tag", and allows for the tracking of the distribution of ejecta material, as well as locating which cells have been injected with energy and momentum. This tag could also used to force refinement in certain simulations, to keep maximal resolution within the supernova bubble. No kinetic energy was initialised, but this is not necessary as the supernova should quickly settle into the attractive ST solution. The initialisation into a Cartesian box could pose problems due to the lack of spherical symmetry (which is more realistic), but this was assumed to have an negligible effect on the resulting remnant due to the small initialisation volume.

The cooling was self-consistent, i.e applied for all conditions, both within the supernova and in the outside medium. The cooling in the outside medium was not done in Martizzi et al. (2015); Kim & Ostriker (2015), which is less realistic but offers pressure equilibrium which is a more controlled setting.

The supernova was tracked with outputs taken with frequency $\Delta t = 0.25$ kyr, giving the variables P, ρ, $\mathbf{u}$, Z and the tag at each cell at the given time. These were then analysed and manipulated using the python module YT (Turk et al. 2011) to get the temperature T, total thermal, kinetic and total energies E_T, E_K, E and the total radial momentum p_r. The energies and momentum were defined as the sum over the respective variable in all cells, with

$$p_{r,i} = m_i \mathbf{u_i} \cdot \hat{\mathbf{r}}_\mathbf{i}, \tag{2.17}$$

$$E_{K,i} = \begin{cases} \frac{p_{r,i}^2}{2m_i}, & \text{if } \mathrm{var}_i > 0 \\ 0, & \text{else} \end{cases} \tag{2.18}$$

$$E_{T,i} = \begin{cases} \frac{3m_i P_i^2}{2\rho_i}, & \text{if } \mathrm{var}_i > 0 \\ 0, & \text{else} \end{cases} \tag{2.19}$$

for cell i, where m_i is the mass and var_i the value of the tag within the cell. The condition that the tag had to be present was used, such that no thermal energy from the medium was accounted for, but still get most of the kinetic energy within a consistent volume.

Values of interest were E and p_r, and the time and radial extent in the transition between the ST-stage and pressure driven snowplow stage t_{ST}. The values for the transition had to be confirmed as it is before here that most of the momentum is gained. These were found via comparisons with the analytic solutions found in section 2.1, via scaling the

Run	dx_{min} (pc)	n (cm^{-3})	Total time of simulations (kyr)
H-n100l610	0.1	100	79.54
H-n100l610nogravnotag	0.1	100	98
H-n100l69	0.2	100	245.87
H-n100l69nograv	0.2	100	245.97
H-n10l610nogravnotag	0.1	10	149.66
H-n10l69	0.2	10	72.93
H-n10l69nogravnotag	0.2	10	97.87
H-n1l610nogravnotag	0.1	1	239.84 (terminated)
H-n1l69nogravnotag	0.2	1	171 (terminated)

Table 2.1: The simulations done of SNe in homogeneous mediums. The parameters varied where the number density of hydrogen n and highest level of refinement (10 or 9) quantified by the resulting dx_{min}. runs which was made with self gravity turned off, or did not enforce refinement with the tag are marked nograv and/or notag. All parameters not mentioned were fixed to values $Z = Z_{\odot}$, $T_0 = 10^4$ K and side length of simulation box $L = 100$ pc. The $n = 1$ cm^{-3} runs were terminated before the final measurements (10 t_{ST}) due to time and storage constraints.

solutions using eqs. (2.5), (2.6) and the relations

$$\rho_{sh} = \left(\frac{\gamma+1}{\gamma-1}\right)\rho_1 \tag{2.20}$$

$$u_{sh} = \frac{2}{(\gamma+1)}U_{sh} \tag{2.21}$$

$$P_{sh} = \frac{2}{(\gamma+1)}\rho_1 U_{sh}^2, \tag{2.22}$$

(see Shu 1991). The equations (2.20)-(2.22) come from the strong shock limit of the Rankine-Hugoniot shock jump conditions (Rankine 1870; Hugoniot 1859), which is the set of equations describing mass, momentum and energy conservation of the pre- to post-shock jump. With the analytic solutions scaled, the time of transition t_{ST} was estimated as the mid point between when the pressure deviates from the analytic solution and when the pressure had reaches the typical PDS shape. The final energy and momentum were also extracted, defined as the values at the time $t = 10t_{ST}$. This definition of the final time is consistent with Kim & Ostriker (2015), and is a good approximation of the final momentum, as at $t = 4 - 5t_{ST}$ most of the momentum has already been gained.

The parameters varied over the simulations are shown in table 2.1. n was varied for comparison with multiple data points in (Kim & Ostriker 2015), while the resolution, inclusion of gravity and forced refinement with the tag being varied to optimise the runs.

2.2.3 Turbulent Medium

Turbulence patch

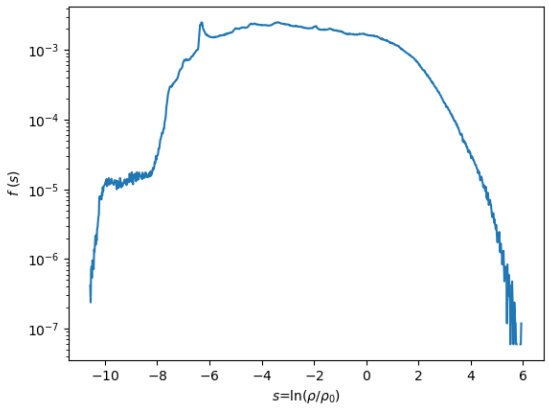

(a) Density probability distribution function $f(\ln(\rho/\rho_0))$, with the density normalised by the average (or initial) density ρ_0.

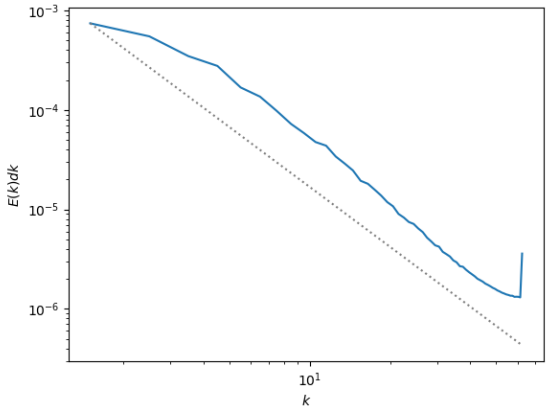

(b) Power spectrum in blue, k^{-2} shown as the dotted line, where k is the wavenumber.

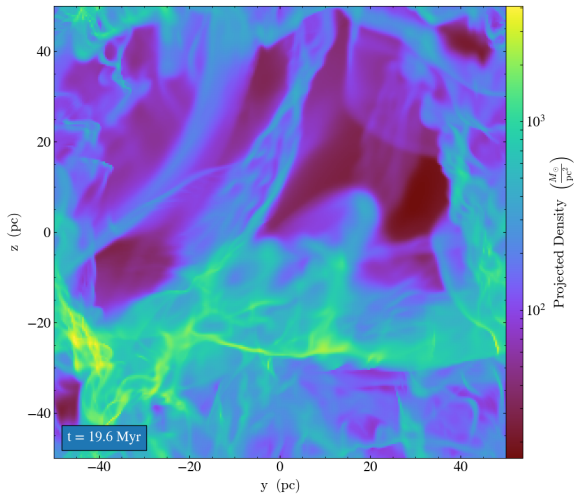

(c) The projected density

Figure 2.2: Density PDF, power spectrum of turbulence and the projected density of turbulence with Mach number 15.

The patch to RAMSES which produced the turbulence (Padoan & Nordlund 1999) did so by computing two forces, which are applied with random scaling over a limited sphere in Fourier space. It then oscillates between the two forces for one turnover cycle (roughly equal to crossing time for the turbulent gas), after which it replaces one of the forces and repeats the process. The amplitude of the force is given by the ratio of the amplitude of the velocity

and turnover time, both of which are set by the user. For the simulations done here, the amplitude of the velocity was set by a Mach number, chosen such that the amplitude would roughly follow the dispersion typical for the size of the cloud; σ (km/s) $= 1.1L^{0.38}$ (pc) $\sim$ 6 km/s for our box (Larson 1981). After running for some cycles of turnover time, this process produces density PDFs similar to those found in Federrath (2013), as shown in figure 2.2. The projected density produces a sheet-like space filling structure, with a power spectrum that roughly follows $E(k)\mathrm{d}k \sim k^{-2}\mathrm{d}k$. However this was only achieved without gravity, as when this was included, the simulation diverged to higher RMS velocities, shallower slopes in the power spectrum and non lognormal density distribution. However as we are concerned about the effects from the type of medium produced without gravity, which reflects the environment in GMC's (Roman-Duval et al. 2010; Federrath 2013), this was deemed acceptable.

Simulations

To detonate a supernovae, similar to what was done for the homogeneous medium, the star particle module in RAMSES was changed to generate a tracer particle at the start of the simulation. This particle was set free in the box while the turbulence was driven for approximately two turnover times. After this point the feedback module in RAMSES was called, which had been changed to insert a second passive scalar, which forced refinement to the maximum level. When the maximum resolution had been reached locally, thermal energy of 10^{51} erg was injected into one of these cells along with some mass, which then initiated the supernova, and the second scalar was removed such that refinement was not forced unnecessarily. At this point, the force driving the turbulence was switched off, such that it would not impact the evolution. While some effects that the forcing module intends to simulate, like gravitational instabilities, would still be affecting the supernova, the implementation of these are not realistic within the bubble, and were therefore turned off. All runs were made with an initial homogeneous number density of $n_0 = 100$ cm^{-3}, as supernovae in GMC's were of interest. Within this, the Mach number was varied, taking values of $\mathcal{M} = 10$ and $\mathcal{M} = 15$ which are the Mach numbers in a typical GMC (Roman-Duval et al. 2010).

To investigate the evolution of energy and momentum of the supernova, both the asymmetry and momentum of the now turbulent medium had to be taken into account. As the medium could cause the bubble to gain an asymmetric morphology, the adiabatic expansion cannot be assumed to be only radial. Therefore instead of measuring the radial momentum p_r, here we instead looked at the magnitude of the momentum in each cell $p = |\boldsymbol{p}|$, and summing over all cells to get the total momentum. A second complication comes when separating the original momentum of the ISM, from the momentum injected by the SN. First it was attempted to do so using the previously mentioned tags, only looking at cells having the tag larger than a certain value. But this proved difficult when only small amounts of the tag was found in the shell of the SN-shock, and this value also changed over time. Another option considered was to do two runs: one with a supernova and one with only decaying turbulence, subtracting the total energy and momentum of the box of the

second from the first. This poses a problem as time steps are variable, meaning that there might not be a comparable time, so instead a fit was made to the decaying turbulence. This was simplified by that both the kinetic energy and momentum decayed linearly over the time scales considered (kyr). This was not always the case with the thermal energy, but this constitutes very little of the total energy, so the decay of this could be taken as linear without affecting the results.

Chapter 3

Results

3.1 Semi-analytic solution to the ST-stage

The pressure, density and velocity radial profiles for the semi-analytic solution are shown in figure 3.1 and are in general agreeance with what is stated in Kim & Ostriker (2015) and Shu (1991), only differing slightly in the value of ξ_0, which was found here as $\xi_0 = 1.1515$ instead of the 1.1517 in Kim & Ostriker (2015).

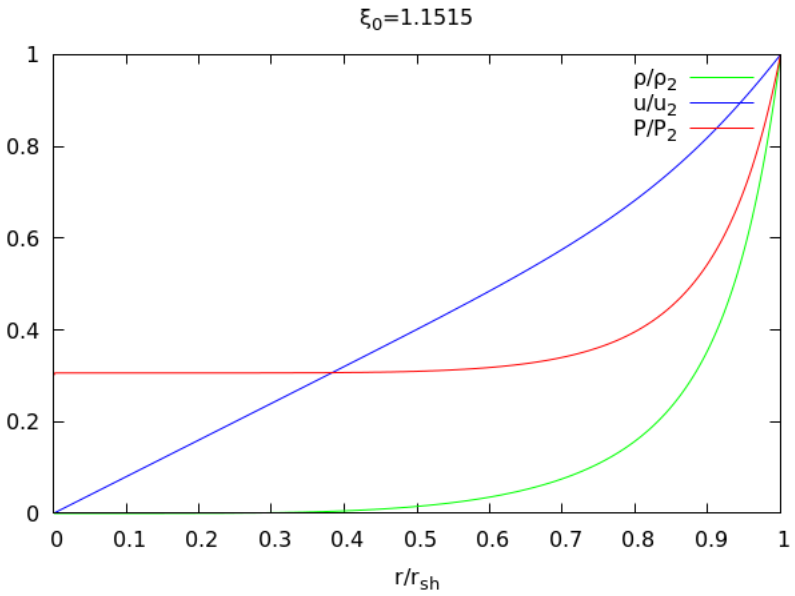

Figure 3.1: The normalized density, velocity and pressure profiles found using the semi-analytic solution.

3.2 Homogeneous Medium

As seen in figure 3.2, the ST, PDS and MDS were all retrieved. This was true for all simulations except for the $n = 1$ cm^{-3} simulations, which were terminated in the transition between PDS and MCS due to time and storage restrictions. The pressure and density (see figure 3.2) were captured in the ST stage and then in the PDS stage, as expected from the cooling, the density was concentrated into a shell with little pressure, while the highest pressure was found inside this shell. The pressure continued to drop, ultimately leaving the cold shell being driven by the conservation of momentum: the MCS stage.

The ST-stages (see figure 3.2 a,b) were realised very close to the semi-analytical solution, with the expected radius of the shock front laying almost exactly at where eq. 2.5 predicts. However it can be noted that the slopes between the shock-front and outside medium are not steep enough to be considered as discontinuities, which is expected in shocks. Some discrepancies might be due to the fact that the the semi-analytical solution assumes a strong shock (i.e. Mach number tending to infinity). Without the strong shock assumption, eq.(2.20)-(2.22) are no longer completely valid, which might explain the lower pressure inside the front. However, it might also be due to numerical artefacts from the initialisation. As the shock was initialised as a cube, some artefacts occur from that the initial velocity lies purely on the Cartesian axes, resulting in a cube shaped bubble in the early stages as can be seen in figure 3.3. These artefacts are removed by diffusion in later times resulting in profiles more similar to the semi-analytic solutions as seen in figure 3.3b. However, some of the initial velocity artefacts appears to be conserved throughout the evolution, causing artefacts behind the shock as seen in figure 3.4b. Similar artefacts in density do also appear in the late stages of the supernova's evolution, as seen in figure 3.3c, an effect credited again to the mapping to a Cartesian grid by Kim & Ostriker (2015).

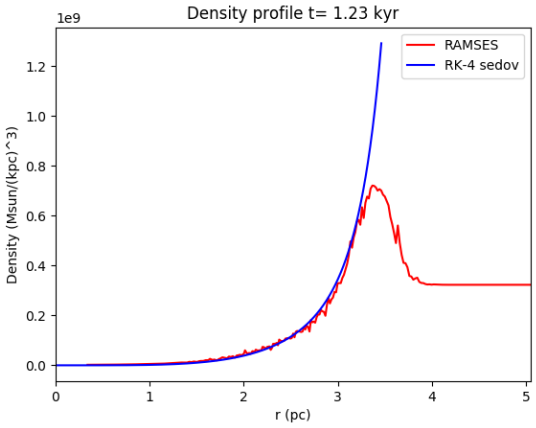

(a) Density profile at ST stage. Both from RAMSES and the semi-analytic.

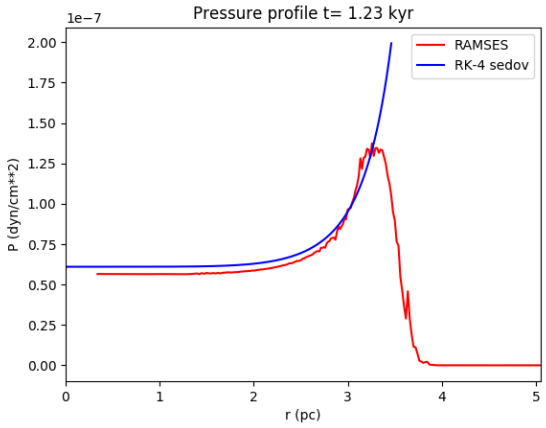

(b) Pressure profile at ST stage. Also with both profiles.

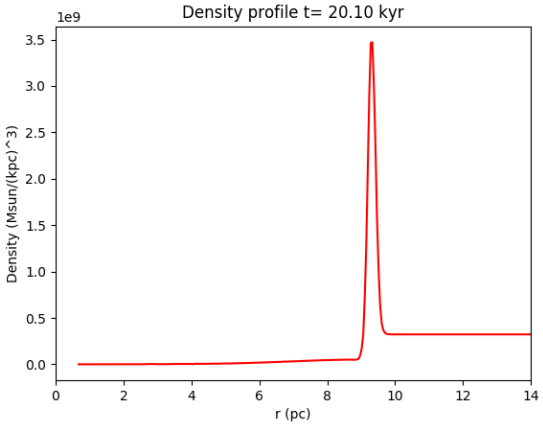

(c) Density profile at PDS stage.

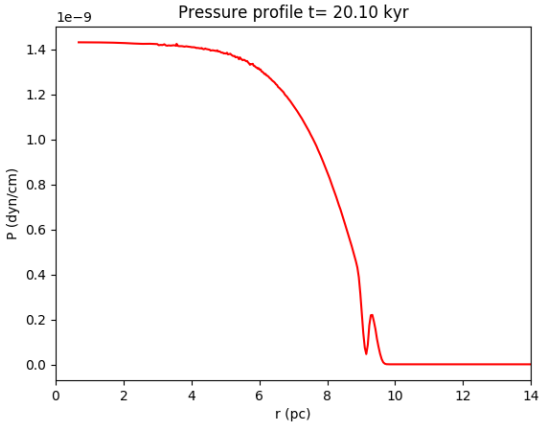

(d) Pressure profile at PDS stage.

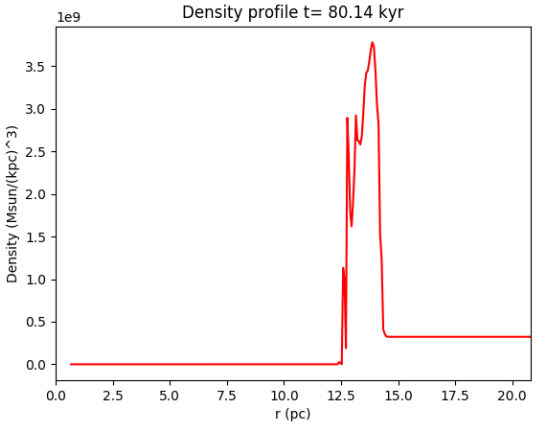

(e) Density profile at MDS stage.

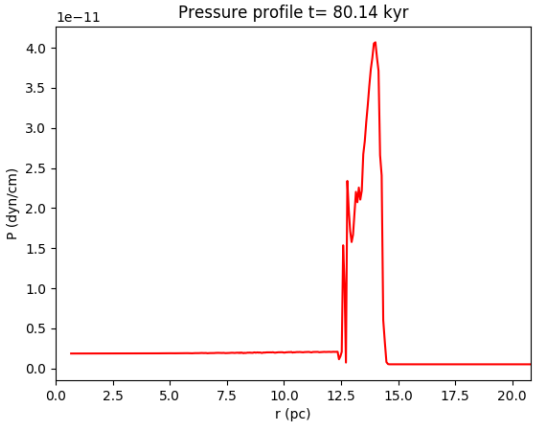

(f) Pressure profile at MDS stage.

Figure 3.2: Averaged profile plots of ρ and P at the ST, PDS and MDS stage from H-n10l69notagnograv run.

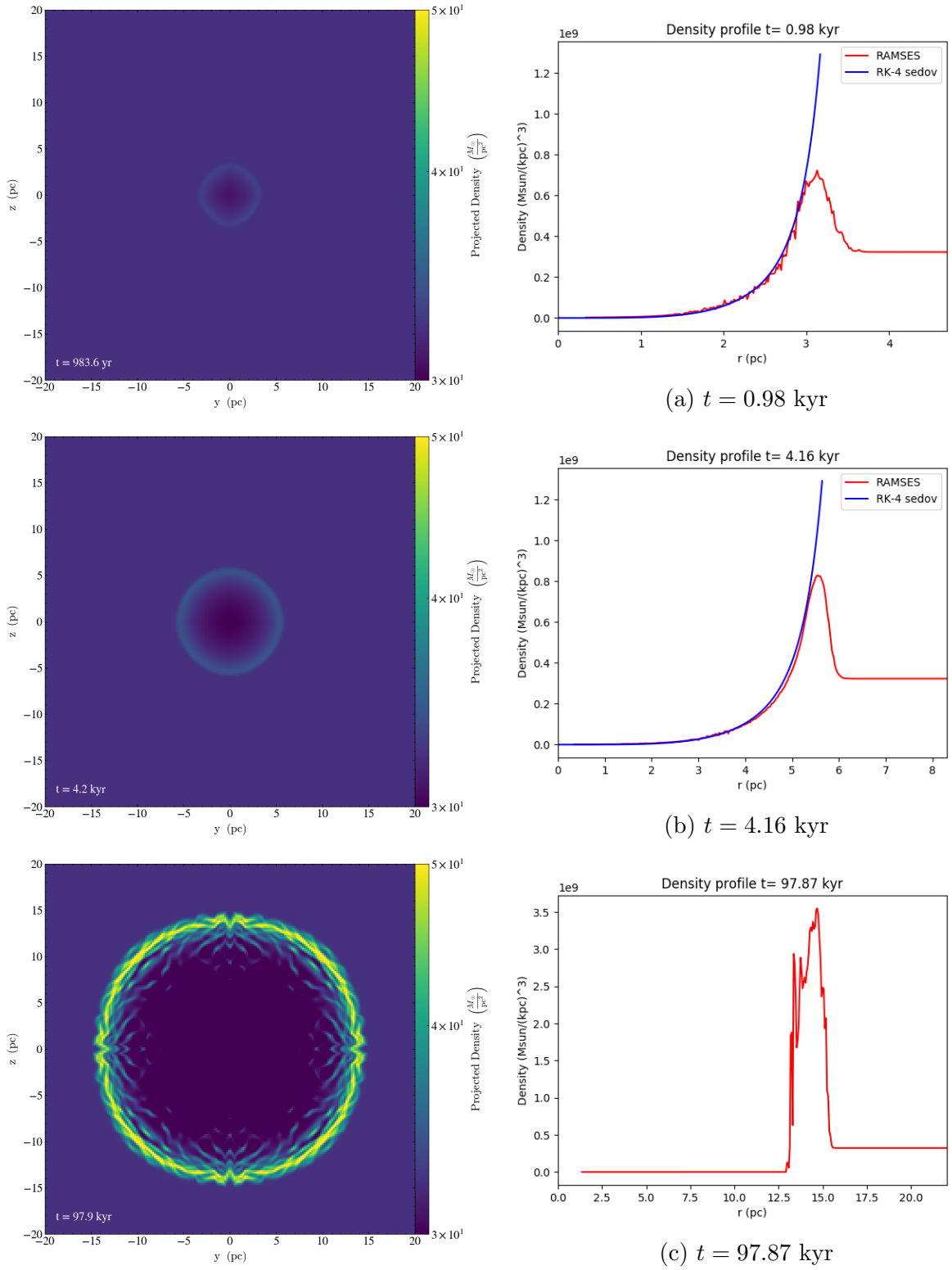

(a) $t = 0.98$ kyr

(b) $t = 4.16$ kyr

(c) $t = 97.87$ kyr

Figure 3.3: Projection plots and averages profile plots of the density for different times in the ST stage. Run H-n10l69notagnograv.

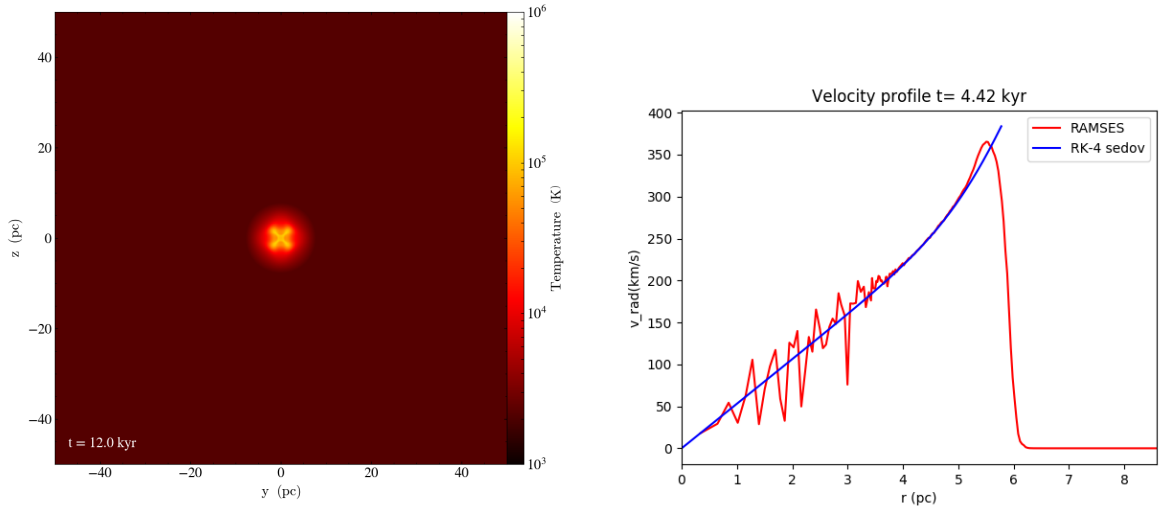

(a) Projection plot of temperature at $t = 12$ kyr. (b) Velocity profile at $t = 4.42$ kyr.

Figure 3.4: Figures showing the artefacts found in temperature and velocity.

Other artefacts found were those of the temperature, which was also subject to the Cartesian artefacts, where at later times the temperature is higher at the diagonals, as seen in figure 3.4a. This artefact in temperature is most likely caused by the velocity, as the temperature is calculated from the total energy, subtracting the kinetic contribution (i.e. v^2). So an artefact in velocity will translate into temperature, as the temperature is a derived quantity. This might however effect the evolution as a whole as the cooling function is temperature dependent, so these artefacts are kept in mind when analysing the evolution of the energy and momentum.

The typical energy and momentum evolutions of the supernovae are shown in figure 3.5, which is consistent with the current understanding of the evolution of SNe bubbles (Martizzi et al. 2015; Kim & Ostriker 2015; Shu 1991). Most of the momentum is gained during the ST-stage, where the most of the energy is conserved. The transition from the ST stages coincides with a decrease in thermal energy. At the end of the PDS stage the momentum and temperature clearly converges, while the kinetic energy continues to decline. The time of the transition between the ST-stage and PDS stages are shown in table 3.1, along with the radius of the shock bubble r_{ST}, total energy E_{ST} and momentum p_{ST} at the transition for all simulations. There appears to be only small little differences between runs with and without gravity and forced refinement with the tag. However, while t_{ST}, r_{ST} and p_{ST} is consistent across all runs for the same density, the energy differs from resolutions of $\Delta x = 0.1$ pc to 0.2 pc, which might be due to the artefacts in the velocity.

Reassuringly, the fitted functions for t_{ST}, r_{ST} and p_{ST} matches those found by Kim & Ostriker (2015), with them being found here for runs with $\Delta x = 0.1$, pc without gravity

or tag refinement as

$$t_{ST} = 34.9 \text{ kyr } n^{-0.56} \quad (3.1)$$
$$(= 40.00 \text{ kyr } n^{-0.59})$$
$$r_{ST} = 19.99 \text{ pc } n^{-0.42} \quad (3.2)$$
$$(= 22.10 \text{ pc } n^{-0.43})$$
$$p_{ST} = 1.79 \cdot 10^5 \text{ M}_\odot \text{ km/s } n^{-0.14} \quad (3.3)$$
$$(= 2.00 \cdot 10^5 \text{ M}_\odot \text{ km/s } n^{-0.15}),$$

where the equalities of in parenthesis are the relations found in Kim & Ostriker (2015), which have generally larger constants than found here. This confirms the weak dependence on the density of all variables, especially p_{ST}. The energy in the runs with $n = 1$ cm^{-3} seems to be lower than that in $n = 10$ cm^{-3}, which should not be the case, but this is likely due to the definition of t_{ST} used here being approximate. But as stated the fitted variables agree well with those found in Kim & Ostriker (2015), so the numerical solutions found here appears valid.

For the final values of the momentum p_{fin} and energy E_{fin} are listed in table 3.2, with the fitted relation of p_{fin} to n found as

$$p_{fin} = 2.6 \cdot 10^5 \text{ M}_\odot \text{ km/s } n^{-0.15} \quad (3.4)$$
$$(= 2.8 \cdot 10^5 \text{ M}_\odot \text{ km/s } n^{-0.17}),$$

where again there is good agreeance with the relation in Kim & Ostriker (2015). In table 3.2, the ratio p_{fin}/p_{ST} for the different results can be also be found. In general Kim & Ostriker (2015) found the ratio $p_{fin}/p_{ST} \sim 1.48$ for all densities considered here, so the $n = 100$ cm^{-3} appears lower, especially for the lower resolutions. This was not the case for $n = 10$ cm^{-3}, where all resolutions gave approximately the same results, and the ratio is consistent with $p_{fin}/p_{ST} \sim 1.46$. This implies that $n = 100$ cm^{-3} is slightly under-resolved even at $\Delta x = 0.1$ pc, however it is still within 10% of what is found in Kim & Ostriker (2015). It can be noted that the accumulated momentum both at t_{ST} and at t_{fin} is an order of magnitude larger than that in the phase of free expansion, $\sim 10^5$ compared to $\sim 10^4$ M$_\odot$ km/s (1 M$_\odot$ ejected at 10^4 km/s), showing the importance of the evolution in the adiabatic stages.

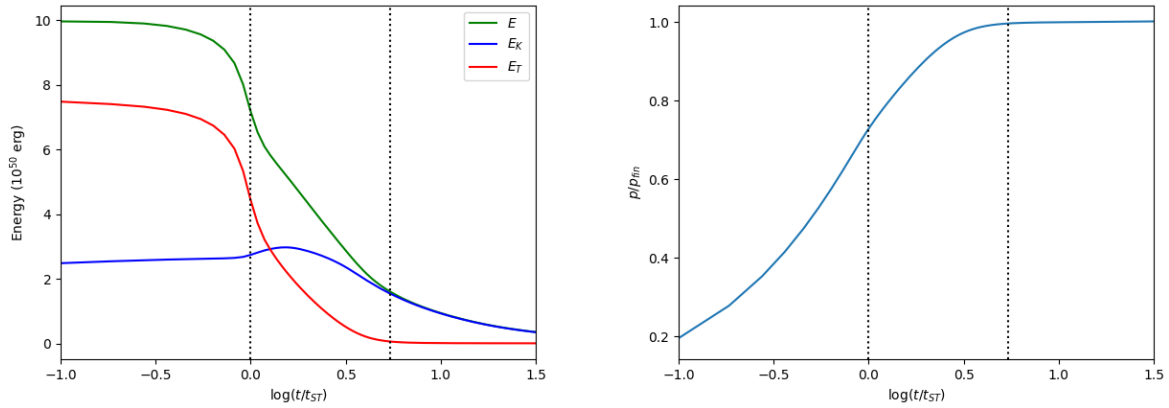

(a) Kinetic E_K, thermal E_T and total Energy E. (b) Total radial Momentum

Figure 3.5: The energy and momentum time evolution of run Run H-n100l610notagnograv. Time is in log scale and normalized to t_{ST}.The transition times from ST to PDS (t_{ST}) and PDS to MCS (t_{PDS}) are indicated in order by the dotted lines.

Table 3.1: The time, radius of the shock bubble, total energy and momentum at the transition from the Sedov-Taylor stage to the pressure driven snowplow stage.

Run	t_{ST} (kyr)	r_{ST} (pc)	E_{ST} (10^{50} erg)	p_{ST} (10^5 $M_\odot$km/s)
h-n100l610	2.7	2.93	7.17	0.970
h-n100l610nogravnotag	2.7	2.93	7.19	0.969
h-n100l69	2.72	2.9	6.52	0.960
h-n100l69nograv	2.72	2.92	6.52	0.960
h-n10l610notagnograv	8.82	7.43	8.37	1.26
h-n10l69	8.93	7.41	8.27	1.27
h-n10l69notagnograv	8.93	7.43	8.26	1.27
h-n1l610notagnograv	36.23	20.26	7.68	1.82
h-n1l69notagnograv	35.25	20.45	7.96	1.81

Table 3.2: Total energy E_{fin}, momentum p_{fin} and the fraction p_{fin}/p_{ST} at $t_{fin} = 10t_{ST}$.

Run	p_{fin} (10^5 $M_\odot$km/s)	p_{fin}/p_{ST}	E_{fin} (10^{49} erg)
h-n100l610	1.33	1.37	9.45
h-n100l610nogravnotag	1.33	1.37	9.40
h-n100l69	1.26	1.32	9.09
h-n100l69nograv	1.26	1.32	9.09
h-n10l610notagnograv	1.85	1.46	9.32
h-n10l69	1.83	1.44	9.92
h-n10l69notagnograv	1.85	1.45	9.92
h-n1l610notagnograv	N/A	N/A	N/A
h-n1l69notagnograv	N/A	N/A	N/A

To conclude the last two sections, we can say that our simulations agree well at the ST-stage with the semi-analytic solutions, and with the results found in Kim & Ostriker (2015). There are some artefacts born from mapping spherical symmetry onto a Cartesian grid, mainly in the velocity and temperature at the critical ST and PDS stages, however these does not appear to affect the results. For instance, the artefacts in temperature were the most apparent in the runs were the tag forced refinement, as otherwise these grids were averaged under the lower resolution, but these runs show no apparent difference from the runs without forced refinement. So as conclusion on the homogeneous numerical simulations, we can say that our supernovae behaves as expected for this idealized case.

3.3 Turbulent Medium

The simulations with turbulent medium gave very complex geometry to the produced shock bubble. In all runs made, the shock bubble followed the path of least resistance, embracing and/or pushing against the high density filaments, causing non-symmetric shapes. At later times Rayleigh-Taylor instabilities could be seen where the shock travelled through density gradients, especially where it was able to penetrate the high density filaments. In figure 3.6, an example of this is shown. In this case the supernova was seeded such that all paths in the slice plot travelled up the density gradient, limiting the growth as the supernova pushed against the nearby filaments, penetrating in one region. In general the shock only managed to destroy the filaments when they were close to the starting point of the supernova, and otherwise it only managed to push into it, favouring low density escape channels.

The complexity also extended into the internal parts of the bubble, where reverse shocks, internal bubbles and turbulence was seen in almost all cases. The reverse shocks were mainly due to the shock colliding with the filaments, while the internal bubbles and turbulence appears to also come from the bubble travelling down density gradients. These types of effects should reheat the interior, which in turn would decrease the total energy in the system via radiation. These internal structures appears to decay over the timespan of the run, but as the shock bubble continues to push against the filaments, more appear.

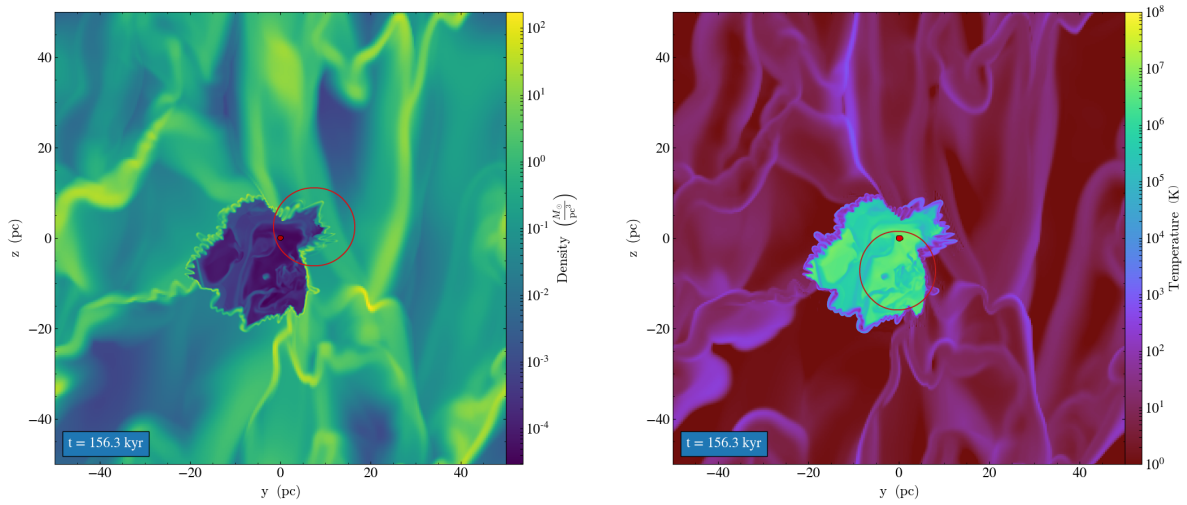

(a) Slice plot of the density

(b) Slice plot of the temperature

Figure 3.6: Figures showing an SNe penetrating dense filament, creating Rayleigh-Taylor instabilities (red circle in a), and also showing complex internal structure with varying temperatures (red circle in b). Initial point of the SNe is indicated by the red dot.

All the effects discussed above could have an impact on the evolution of the shockwave. When internal shocks are created, mass is redistributed into the internal bubble, which could affect all evolutionary stages. In the next part of this section we'll to estimate this.

As seen in figure 3.7, the evolution of the energy and momentum followed the same type of evolution as in the homogeneous case. The energy remains approximately constant at the early stages (although less so than the homogeneous case), while the momentum increases. At some point the thermal energy starts to decrease rapidly, followed by the kinetic energy, similar to the ST-PDS transition. The momentum does seem to decrease at the end of the evolution, something which is not predicted, however at least for the early times, it seems as if the general SNe evolution holds. Due to the asymmetry, defining evolutionary stages is less obvious, as different regions of the supernova could vary widely in density, leading to different transition times. Instead we chose to compare to homogeneous cases of mean densities at the time of their transition $t_{ST,i}$, where the relation between the expected homogeneous momentum $p_{ST,i}$ was compared to the actual momentum p_i. The expected values were estimated using the found relations (3.1,3.3). Three different mean densities were used:

- Initial density: Here the pre-blast density of the cell in which the supernova energy was ejected was used to estimate the time ST-PDS transition t_{ST} using the found relation (3.1). Indexing: $t_{ST,0}$, $p_{ST,0}$, p_0.

- Local mean density: Using the initial density above, the radius of the ST-PDS transition was estimated using eq.(3.2). The mean density in this sphere was then used to

find a new radius using the same method. This was iterated until the mean density converged, which then was used to find t_{ST}. Indexing: $t_{ST,mean}$, $p_{ST,mean}$, p_{mean}.

- Global mean density: This took the initial mean density of the simulation $n = 100$ cm^{-3} to estimate t_{ST}. Indexing $t_{ST,100}$, $p_{ST,100}$, p_{100}.

The reasoning for the inclusion of the initial density is, as seen before, that the early period of SNe remnants evolution is important and contributes most of the momentum. Therefore, the initial density might be an indication of the early development. However, as we expect the density to yield a gradient, the local mean could give a better approximation, specifically the end of the Sedov-Taylor stage. The local mean is also a good indication of how well galactic simulations could resolve the supernovae, as their resolution often reaches down to 10-100 pc (Agertz et al. 2013), the lower end of which would be the scale we expect the estimates to converge at. Lastly the global mean is used as a straight comparison between the box with and without turbulence, and also covers the lower range of resolutions in galactic simulations and the higher end of cosmological simulations.

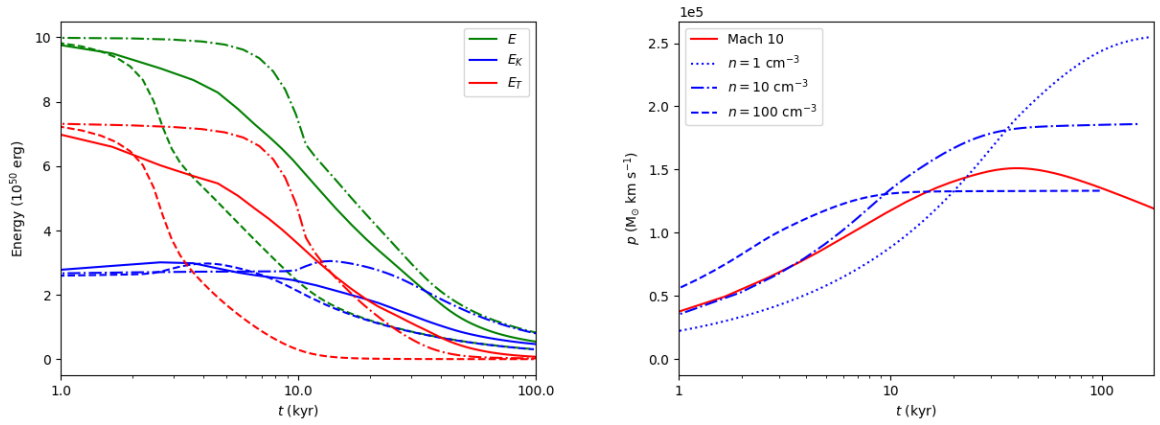

(a) Energy (b) Momentum

Figure 3.7: The energy and momentum evolution of a Mach 10 driven turbulence simulation in solid lines. Initial density at the supernova was found as $n = 30.77$ cm^{-3}, with a local mean of $n = 45.64$ cm^{-3}. Compared to $n = 100$ (dashed), $n = 10$ (dash dotted) and $n = 1$ cm^{-3} (dotted).

The momentum at t_{ST} and the fraction p/p_{ST}, where p_{ST} is the expected momentum from equation (3.3), are found in appendix B in table B.2. In general, both the local and global mean densities predicted momenta $\sim 20 - 30$ % higher than was found, with $n = 100$ cm^{-3} almost consistently over predicting by above 30 %. This can have at least two interpretations, the first being that our methods underestimates the time of the actual equivalent homogeneous ST to PDS transition. This would overestimate momentum, as while the lower densities have higher momentum at certain stages, they gain this over longer

time periods. The second interpretation is that the shock and medium do not retain the momentum gained, instead it is annihilated in collisions. The first is the probable reason for the global mean, while the second applies to the local mean and initial density as can be seen in figure 3.7b. Here the bubble first follows the evolution of the homogeneous case with the initial density $\sim$ 30 cm^{-3} (slightly higher than the 10 cm^{-3} shown), but soon starts deviating from it. As the homogeneous case starts to converge, the turbulent reaches its maximum, after which it starts to decrease. This can be also be seen from the energy in figure 3.7a, where energy, while more resembling the $n = 10$ cm^{-3} case, suffers from energy losses earlier, and is lesser for most of the early evolution.

The last comparison with the homogeneous case made here is that of the peak momentum p_{max} in the turbulent medium, with the final momentum found in section 3.2. As the momentum starts to decline after some time, we make the comparisons with the maximum momentum p_{max} found. Here the three density references, the initial, local mean and global mean densities were again used. The ratio between p_{max} and the estimated final momenta $p_{fin,i}$ are tabulated in table B.3 in appendix B. Surprisingly, the p_{max} found appears to be comparable to the estimated $p_{fin,mean}$, averaging around 1 for $\mathcal{M} = 15$ and 1.16 for $\mathcal{M} = 10$, in spite of being decisively lower at previous times. The comparison with the global mean density was consistently higher, as expected with the starker density differences. This is still within $\sim$ 30 % of the expected momentum in the homogeneous case, so the difference is similar to what was found by Martizzi et al. (2015); Kim & Ostriker (2015).

The reason for the more comparable $p_{max}/p_{fin,mean}$ might be because of the escape channels. As the bubble gets stuck in the filament and expands into the low density regions, it injects much of its momentum into low density regions. As the shock couples to these lower densities it would gain higher momentum, as lower densities lengthen the different evolutionary stages. However the momentum appears to decay, the reason for which is yet to be determined, but might be due to the shock continuing to travel with increasing density gradients, heating the material which then cools within the high density shell. One can also imagine that the decay of energy and momentum which is contained within the bubble could cause the decrease. This however should heat the bubble, which is not apparent in the energy evolution, but this does not exclude the possibility of this explanation as the increases may be small, yet numerous such that it appears continuous. Finally the decrease might just be the annihilation of momenta as the bubble might travel against the velocity of the medium. As there is no previous work with high resolution SNe in turbulent media, this is new territory for future analysis.

Chapter 4

Discussion

On the topic of the work done here, there are many things to improve upon. In real GMCs one would expect active star formation, the resulting mass loss and radiation of which might affect the density distribution. Also, as the star particle generated here was stationary, and not affected by gravity, a realistic correlation between stars and gas has not been considered. However, given that the problem is already complex, these aspects are considered beyond the scope of this project.

As most comparisons made are within reasonable limits of the expected value of the homogeneous case for both a local and global mean density, there is an argument to be made that the momentum injection from SNe is largely independent of the surrounding structure, only having a weak dependence on the density. This result is similar to what is found in Martizzi et al. (2015); Kim & Ostriker (2015), however this is the first time it has been confirmed in a controlled turbulent environment, with realistic velocity and density distributions based on the observed ISM. This gives us confidence in the sub-grid models shown in full in Martizzi et al. (2015); Kim & Ostriker (2015), and in part here.

However, while the maximum momenta found in both Mach regimes are slightly greater than the homogeneous case of a global mean density, this soon changes as the momentum decreases, something which is not captured at either scale. The time scale of this appears to be long, and not fully simulated here. Previous studies, which did let their SNe expand for longer did not show this at any stage of the evolution (Martizzi et al. 2015; Kim & Ostriker 2015), however as stated these did not include a full turbulence model, as used here. If it is found that the decrease is happening on large enough time and spatial scales for large scale simulations to capture, then the generality of the maximum (or final) momentum seen here and in previous work is good news for the field of galaxy modelling where estimates of the final injected momentum would still hold for unresolved yet complicated flows. However, if the decrease is due to local, small scale effects it would not be accurately captured, and could therefore be an issue.

It has previously been thought that supernovae alone cannot generate the galactic winds and outflows required to properly regulate star formation (Agertz et al. 2013). But with their results Kim & Ostriker (2015) argued that this was mainly due to numerical restrictions and not an astrophysical effect. However with the decaying SNR momentum

found here, this might be challenged again if the time or spatial scale of the decay is short. But as neither the cause, the scales, nor full effect of the decay is known, and has not been analysed fully, further analysis is left for future work.

The tendency of the bubble to follow the density gradients created shocks that extended in some cases up to 50-60 pc. While this is not quantified in this report, it can have implications on the outflows of gas from the galactic discs. The results imply outflows of diffuse gas from GMCs, as the shock mostly couples to the low density regions, something which is difficult to capture in large scale galaxy simulations, where the feedback is instead coupled to more mass due to low resolution. The denser filaments, however, remain mostly intact over the time scales considered, requiring multiple supernovae in order for the denser gas to escape. These effects could have implications on galaxy evolution, where feedback is important for the prediction of galaxy masses and sizes (Agertz & Kravtsov 2016). As the dense filaments appears to survive the supernova, the findings here imply that the quenching of star formation caused by single SNe is not very effective, as the filaments would be the regions of star formation. In reality one would expect stellar clusters to drift away slightly from the GMC (Renaud et al. 2013), and not being in the centre of the GMC as in the realization here. One also expects radiation from stars to create a diffuse region, which would surround any resulting SNe. However, these conditions would amplify the effects seen here, as they can give rise to more low density regions and escape channels for the SNe, which therefore may have an even lesser effect on the filaments.

Both the decaying turbulence and the intact filaments invites for further simulations of multiple SNe. In reality stars would form in clusters, and as the more massive stars starts reach the end of their lifespan, a sequence of SNe occur and the resulting shockwaves from these forms a superbubble (SB). The nature of SBs are important, as the momentum injection per supernova, the outflow of gas and the heating of the ISM caused by these are key ingredients for many galactic models Keller et al. (2014); McKee & Ostriker (1977). In a continuation their work cited frequently here Kim & Ostriker (2015) found that the interactions between the SNe reduced the momentum per supernovae, something that was not supported by Gentry et al. (2017), however these used a simpler 1D model. The decreasing momentum found here would support Kim & Ostriker (2015), but whether this effect remains with successive SNe is still unknown. With many of our filaments still intact, the inclusion of multiple SNe could be able to break these and allow for more outflows. However with several massive stars, we would require higher gas densities and therefore may require more dense filaments, so this is not a simple extrapolation and is an interest for future work.

Chapter 5

Conclusion

Feedback from massive stars plays a crucial role in galaxy formation, with the energy and momentum injection being one the main processes regulating star formation, along with driving turbulence and galactic outflows. Among the processes of stellar feedback, supernovae are thought to be one of the dominant. However, the resolution required to resolve the early adiabatic phases of SNe, which are responsible for most of the momentum generation, often forces galactic and cosmological simulators to adopt sub-grid models, or suffer from problems such as over-cooling in the early stages. Therefore small scale, controlled simulations as done in previous works (Martizzi et al. 2015; Kim & Ostriker 2015; Thornton et al. 1998; Haid et al. 2016) are needed to quantify the momentum injection from SNe into the ISM at larger scales. However none of these have fully simulated the turbulent nature of the ISM, and have instead taken static realisations of the general structure. In this work we have chosen a model of driving active supersonic turbulence, to study how the high velocities and resulting gas filaments affect the evolution and momentum injection of SNe. This is the first controlled experiment of its kind of which we know, so our supernovae were tested against the semi-analytic solution of the Sedov-Taylor stage and previous work.

Our results can be summarised as follows

- By solving the set of coupled ODEs of normalized variables, corresponding to the spherically symmetric Euler equations, the density, pressure and velocity profiles of an idealized point blast was recovered.

- In the case of homogeneous media, the semi analytic solution was recovered in full hydrodynamical AMR simulations using RAMSES, confirming the modelling of the Sedov-Taylor stage. The simulations had several numerical artefacts due to mapping spherical symmetry onto a Cartesian grid, however this had a negligible effect on the evolution of the blast wave.

- With the inclusion of atomic cooling, the stages of SNe evolution was recovered. The time, radius and momentum at the transition from the Sedov-Taylor to the pressure driven snowplow stage was found in good agreement with results from Kim & Ostriker

(2015) as

$$t_{ST} = 34.9 \text{ kyr } n^{-0.56}$$
$$r_{ST} = 19.99 \text{ pc } n^{-0.42}$$
$$p_{ST} = 1.79 \cdot 10^5 \text{ M}_\odot \text{ km/s } n^{-0.14}.$$

The momentum here is one order of magnitude larger than the momentum of the initial ejecta and the phase of free expansion, which shows that understanding the momentum generation throughout the different stages of SNe evolution is important.

- The final momentum injected into the ISM was found in the homogeneous case as

$$p_{fin} = 2.6 \cdot 10^5 \text{ M}_\odot \text{ km/s } n^{-0.15},$$

also in excellent agreeance with Kim & Ostriker (2015). This confirmed that most of the momentum is gained in the Sedov-Taylor adiabatic phase, and that the realization of SNe blast waves here is valid.

- In the case of turbulent medium, the shock bubbles generally shows complex geometry as the shock prefers the path of least resistance. This preference appears to indicate anisotropic outflows of diffuse gas from single SNe, with the momentum coupling with larger scales (up to ~ 50 pc), something which is not captured in large scale simulations where the momentum couples to the higher homogeneous densities of single cells. In addition to this, several features such as reflective shocks and turbulence can be seen inside the bubble, especially where in regions were the bubble is interacting with high density filaments.

- Reassuringly, the general evolution of momentum and energy is at large consistent with the homogeneous case, only differing within $\sim 10 - 30$ % in the maximum momentum. This momentum does however decrease, something not seen in the homogeneous case were the final stage conserves momentum. The general characteristics of this decrease is however not quantified here and is left for future studies.

Bibliography

Agertz, O. & Kravtsov, A. V. 2016, The Astrophysical Journal, 824, 79

Agertz, O., Kravtsov, A. V., Leitner, S. N., & Gnedin, N. Y. 2013, The Astrophysical Journal, 770, 25

Burgers, J. 1948, in Advances in Applied Mechanics, Vol. 1, A Mathematical Model Illustrating the Theory of Turbulence, ed. R. V. Mises & T. V. Kármán (Elsevier), 171 – 199

Creasey, P., Theuns, T., Bower, R. G., & Lacey, C. G. 2011, Monthly Notices of the Royal Astronomical Society, 415, 3706

Federrath, C. 2013, Monthly Notices of the Royal Astronomical Society, 436, 1245

Gentry, E. S., Krumholz, M. R., Dekel, A., & Madau, P. 2017, Monthly Notices of the Royal Astronomical Society, 465, 2471

Godunov, S. K. 1959, Mat.Sb.(N.S.), 47, 271

Haid, S., Walch, S., Naab, T., et al. 2016, Monthly Notices of the Royal Astronomical Society, 460, 2962

Hugoniot, H. 1859, Journal de l'ecole polytechnique, 58

Keller, B. W., Wadsley, J., Benincasa, S. M., & Couchman, H. M. P. 2014, Monthly Notices of the Royal Astronomical Society, 442, 3013

Kim, C.-G. & Ostriker, E. C. 2015, The Astrophysical Journal, 802, 99

Larson, R. B. 1981, Monthly Notices of the Royal Astronomical Society, 194, 809

Mac Low, M.-M. & Klessen, R. S. 2004, Reviews of Modern Physics, 76, 125

Martizzi, D., Faucher-Giguère, C.-A., & Quataert, E. 2015, Monthly Notices of the Royal Astronomical Society, 450, 504

McKee, C. F. & Ostriker, E. C. 2007, Annual Review of Astronomy and Astrophysics, 45, 565

McKee, C. F. & Ostriker, J. P. 1977, The Astrophysical Journal, 218, 148

Padoan, P. & Nordlund, Å. 1999, The Astrophysical Journal, 526, 279

Rankine, W. J. M. 1870, Philosophical Transactions of the Royal Society of London, 160, 277

Renaud, F., Bournaud, F., Emsellem, E., et al. 2013, Monthly Notices of the Royal Astronomical Society, 436, 1836

Roman-Duval, J., Jackson, J. M., Heyer, M., Rathborne, J., & Simon, R. 2010, The Astrophysical Journal, 723, 492

Sharp, D. 1984, Physica D: Nonlinear Phenomena, 12, 3

Shu, F. 1991, The Physics of Astrophysics: Gas dynamics, Series of books in astronomy (University Science Books)

Stinson, G., Seth, A., Katz, N., et al. 2006, Monthly Notices of the Royal Astronomical Society, 373, 1074

Teyssier, R. 2002, Astronomy and Astrophysics, 385, 337

Thornton, K., Gaudlitz, M., Janka, H.-T., & Steinmetz, M. 1998, The Astrophysical Journal, 500, 95

Turk, M. J., Smith, B. D., Oishi, J. S., et al. 2011, The Astrophysical Journal Supplement Series, 192, 9

Appendix A

Solving the coupled ODE's

Reorganizing the coupled odes of eqs. (2.1)-(2.3), such that they are structured in terms of derivatives, we find

$$\left(\frac{2v}{\gamma_+}-1\right)\xi\frac{\mathrm{d}\alpha}{\mathrm{d}\xi}+\frac{2\alpha}{\gamma_+}\xi\frac{\mathrm{d}v}{\mathrm{d}\xi}+\frac{6}{\gamma_+}\alpha v=0 \tag{A.1}$$

$$\frac{2}{5}\left(\frac{2v}{\gamma_+}-1\right)\xi\frac{\mathrm{d}v}{\mathrm{d}\xi}+\frac{2}{5\alpha}\frac{\gamma_-}{\gamma_+}\xi\frac{\mathrm{d}p}{\mathrm{d}\xi}+2\left(\frac{2\gamma v}{\gamma_+}-1\right)\left(p+\alpha v^2\right)=0 \tag{A.2}$$

$$\begin{aligned}\frac{2}{5}\left(\frac{2v}{\gamma_+}-1\right)v^2\xi\frac{\mathrm{d}\alpha}{\mathrm{d}\xi}+\frac{4}{5}\left[\frac{1}{\gamma_+}\left(\gamma p+3\alpha v^2\right)-\alpha v\right]\xi\frac{\mathrm{d}v}{\mathrm{d}\xi}+\frac{2}{5}\left(\frac{2\gamma v}{\gamma_+}-1\right)\xi\frac{\mathrm{d}p}{\mathrm{d}\xi}+\\ 2\left(\frac{2\gamma v}{\gamma_+}-1\right)p+2\left(\frac{2v}{\gamma_+}-1\right)\alpha v^2=0,\end{aligned} \tag{A.3}$$

where $\gamma_\pm=\gamma\pm1$. From this we can see that the $\mathrm{d}\alpha/\mathrm{d}\xi$ terms in eqs A.1 and A.3 shares a common factor, so subtracting $2/5v^2\cdot$A.1 from A.3 cancels these terms and after simplifying we get

$$\left(\frac{2v}{\gamma_+}-1\right)\xi\frac{\mathrm{d}\alpha}{\mathrm{d}\xi}+\frac{2\alpha}{\gamma_+}\xi\frac{\mathrm{d}v}{\mathrm{d}\xi}+\frac{6}{\gamma_+}\alpha v=0 \tag{A.4}$$

$$\frac{2}{5}\left(\frac{2v}{\gamma_+}-1\right)\xi\frac{\mathrm{d}v}{\mathrm{d}\xi}+\frac{2}{5\alpha}\frac{\gamma_-}{\gamma_+}\xi\frac{\mathrm{d}p}{\mathrm{d}\xi}+2\left(\frac{2\gamma v}{\gamma_+}-1\right)\left(p+\alpha v^2\right)=0 \tag{A.5}$$

$$\begin{aligned}\frac{4}{5}\left[\frac{1}{\gamma_+}\left(\gamma p+2\alpha v^2\right)-\alpha v\right]\xi\frac{\mathrm{d}v}{\mathrm{d}\xi}+\frac{2}{5}\left(\frac{2\gamma v}{\gamma_+}-1\right)\xi\frac{\mathrm{d}p}{\mathrm{d}\xi}+\\ 2\left(\frac{2\gamma v}{\gamma_+}-1\right)p+2\left(\frac{4v}{5\gamma_+}-1\right)\alpha v^2=0.\end{aligned} \tag{A.6}$$

We now cancel the $\mathrm{d}p/\mathrm{d}\xi$ term in eq A.6 by subtracting

$$\text{A.6}-\frac{\gamma_+\alpha}{\gamma_-}\left(\frac{2\gamma v}{\gamma_+}-1\right)\text{A.5}, \tag{A.7}$$

which after some algebra gives

$$\frac{4}{5}\left[\frac{1}{\gamma_+}\left(\gamma p + 2\alpha v^2 - 2\frac{\gamma\alpha v^2}{\gamma_-}\right) - \left(1 - \frac{\gamma_+}{\gamma_-}\right)\alpha v - \frac{\gamma_+}{\gamma_-}\frac{\alpha}{2}\right]\xi\frac{\mathrm{d}v}{\mathrm{d}\xi} - \frac{\gamma_+}{\gamma_-}\alpha v + \frac{6}{5}\left(\frac{2\gamma v}{\gamma_+} - 1\right)p + 2\left[\left(\frac{4v}{5\gamma_+} - 1\right) - \frac{4v}{5\gamma_+\gamma_-} + \frac{2/5 + \gamma}{\gamma_-}\right]\alpha v^2 = 0. \tag{A.8}$$

Equation A.8 now has $\mathrm{d}v/\mathrm{d}\xi$ independent on the other derivatives, such that it can be solved to get equation 2.14. Now equation (A.1) could be solved for $\mathrm{d}\alpha/\mathrm{d}\xi$ and equation (A.5) for $\mathrm{d}p/\mathrm{d}\xi$ to get equations (2.15) and (2.16) respectively.

Appendix B

Simulations in turbulent medium.

Table B.1: The initial and local mean density of all simulations. Simulations are named after the Mach number used, with an iterative digit separating them

run (Mach+run number)	n_0 (cm^{-3})	n_{mean} (cm^{-3})
M10-1	30.77	45.64
M10-2	4.58	82.62
M10-3	1.11	9.93
M10-4	5.57	19.18
M10-5	1.47	19.28
M10-6	103.02	757.07
M15-1	7.45	45.11
M15-2	0.25	10.49
M15-3	0.70	4.40
M15-4	3.92	104.2
M15-5	48.37	82.82

Table B.2: The estimated t_{ST}s in kyr using the different methods, with the found momentum p at these estimates in 10^5 $M_\odot$km/s, and the fraction p/p_{ST} at these times for all simulations.

run (Mach+run number)	$t_{ST,0}$	p_0	$p_0/p_{ST,0}$	$t_{ST,mean}$	p_{mean}	$p_{mean}/p_{ST,mean}$	p_{100}	$p_{100}/p_{ST,100}$
M10-1	5.05	1.07	0.96	4.04	0.96	0.91	0.76	0.79
M10-2	14.80	1.32	0.91	2.90	0.67	0.69	0.64	0.67
M10-3	32.88	1.69	0.96	9.56	0.91	0.70	0.40	0.42
M10-4	13.24	1.21	0.86	6.59	0.92	0.77	0.54	0.57
M10-5	28.07	1.55	0.91	6.57	0.80	0.67	0.49	0.51
M10-6	2.56	0.76	0.80	0.83	0.49	0.67	0.77	0.80
M15-1	11.24	1.21	0.89	4.07	0.80	0.75	0.63	0.66
M15-2	76.46	1.66	0.77	9.26	0.94	0.72	0.40	0.42
M15-3	42.70	1.70	0.91	15.12	1.19	0.81	0.38	0.40
M15-4	16.13	1.30	0.88	2.54	0.61	0.64	0.62	0.65
M15-5	3.91	0.99	0.94	2.89	0.86	0.88	0.81	0.85

Table B.3: The fraction of the peak momentum for each run over the estimated final momentum in the homogeneous case, using different methods.

run (Mach+run number)	t_{max}	$p_{max}/p_{fin,0}$	$p_{max}/p_{fin,mean}$	$p_{max}/p_{fin,100}$
M10-1	52.39	1.10	1.16	1.31
M10-2	38.82	0.74	1.13	1.16
M10-3	101.6	0.84	1.16	1.63
M10-4	53.46	0.84	1.01	1.29
M10-5	110.06	0.90	1.31	1.67
M10-6	50.41	1.20	1.61	1.19
M15-1	35.10	0.81	1.05	1.18
M15-2	54.70	0.54	0.94	1.30
M15-3	54.13	0.64	0.84	1.32
M15-4	21.59	0.63	1.02	1.02
M15-5	24.76	1.03	1.11	1.14